TITLE

Characterization of Novel Graphene-based Microporous Layers for Polymer Electrolyte Membrane Fuel Cells Operating under Low Humidity and High Temperature

AUTHORS

Marco Mariani[a], Saverio Latorrata[a], Stefano Patrignani[a], Paola Gallo Stampino[a], Giovanni Dotelli[a]

POSTAL ADDRESS

[a]Department of Chemistry, Materials and Chemical Engineering ‘‘G. Natta’’, Politecnico di Milano, Piazza Leonardo da Vinci 32, 20133 Milano, Italy

EMAIL ADDRESS

marco.mariani@polimi.it

saverio.latorrata@polimi.it

stefano.patrignani@mail.polimi.it

paola.gallo@polimi.it

giovanni.dotelli@polimi.it

CORRESPONDING AUTHOR

marco.mariani@polimi.it

ABSTRACT

Water management is one of the major issues hindering the employment of Polymer Electrolyte Membrane Fuel Cells on a large scale. Microporous layers are fundamental for water removal from the cathode, oxygen mass transfer and electrolyte hydration. In this paper, we have employed multiple carbon phases in the MPL composition to identify possible strategies for cell performance improvement at critical conditions such as high temperature and low relative humidity. In particular, we have employed a series of graphene-based particles, in addition to conventional carbon black, because of their excellent electrical and thermal conductivities. Moreover, mixed compositions have been tested to assess possible synergic effects between the two phases. We have determined which properties are responsible for performance improvements at 80 °C and relative humidity of 60 % and how MPLs morphological and microstructural features could be tuned in order to increase mass transfer while preserving the electrolyte

membrane hydration. Promising results have been obtained and specific morphological properties of graphene nanoplatelets have been identified for a possible optimization of the MPL, however the samples produced are still at an early-stage development and further improvements are needed.

KEYWORDS

Polymer electrolyte membrane fuel cells (PEMFC)

Microporous layer (MPL)

Gas diffusion layer (GDL)

Permeability

Graphene nanoplatelets

Carbon black

HIGHLIGHTS

- Microporous layers with carbon black, graphene and carbon nanotubes were prepared.
- Crack-free MPLs were achieved with the use of graphene nanoplatelets.
- MPLs permeability was analysed and correlated to optimal T and RH.
- Different carbonaceous phases almost have no effect on electrical conductivity.
- Ohmic and mass transfer losses strongly depended on the MPLs morphology.

NOMENCLATURE

A	Surface area (m^2)
d	Pore diameter (m)
g	Gravitational acceleration ($m\ s^{-2}$)
h	Height (m)
K	Permeability coefficient (m^2)
m	Mass (kg)
L	Thickness (m)

P	Pressure (Pa)
P_c	Capillary Pressure (Pa)
P_{cur}	Vapour pressure on a curved surface (Pa)
P_{flat}	Vapour pressure on a flat surface (Pa)
r	Meniscus radius (m)
R	Ideal gas constant (J K^{-1} mol^{-1})
R_i	In-plane resistance (Ω)
R_t	Through-plane resistance (Ω)
RH	Relative humidity
t	Time (s)
T	Temperature (K)
V_m	Molar volume (m^3 mol^{-1})

GREEK SYMBOLS

γ	Surface tension at the liquid-vapour interface (N m^{-1})
λ_{air}	Air mean free path (m)
μ	Viscosity (Pa s)
ρ	Density (kg m^{-3})
ρ_i	In-plane resistivity (Ω m)
ρ_t	Through-plane resistivity (Ω m)
θ	Liquid-solid contact angle (°)

ABBREVIATIONS

BP	Bipolar Plate
CB	Carbon Black
CL	Catalyst Layer
CNT	Carbon Nanotube
DI	Deionized Water
EG	Exfoliated Graphite
FEP	Fluorinated Ethylene Propylene
GDL	Gas Diffusion Layer
GDM	Gas Diffusion Medium
GNP-M	Graphene Nanoplatelets – Medium size
GNP-S	Graphene Nanoplatelets – Small size
IPA	Isopropyl Alcohol
MEA	Membrane Electrode Assembly
MIP	Mercury Intrusion Porosimetry
MPL	Microporous Layer
OCV	Open Circuit Voltage
PEMFC	Polymer Electrolyte Membrane Fuel Cell
SCA	Static Contact Angle
SEM	Scanning Electron Microscopy

1 INTRODUCTION

The growing concern for environmental pollution and climate change is pushing for a dramatic turn in energy production and management strategies on a global scale. In this scenario, alternatives to traditional power production systems are quickly arising. According to a recent forecast [1], the fuel cell

market is projected to grow by at least 500% by 2025 and Polymer Electrolyte Membrane Fuel Cells (PEMFCs) represent more than 75% of this segment. Despite the rapid diffusion of this type of technology, large improvements are still needed to make these fuel cells cost-effective (currently PEMFCs are over $20/kW more expensive than required for a 500k/year product volume), durable and efficient, thus promoting their adoption in both the stationary and the automotive industries [2-8].
The Gas Diffusion Medium (GDM) is a fundamental component that increases the efficiency of the device by contributing to different mechanisms occurring in the cell:

- it helps providing a more homogeneous flow of gas from the bipolar plates channels to the catalyst layers (CLs), which increases the catalytic sites coverage and usage [9-10];
- it improves the ohmic contact between the electrodes and the bipolar plates [10];
- it improves the thermal management inside the cell and reduces the risk of formation of thermal gradients due to heat produced by the reactions, thus preventing localised deformations and distortions [11-21];
- it provides mechanical support to the membrane electrode assembly (MEA) and reduces the CLs mechanical degradation due to direct contact with the bipolar plates (BPs);
- it improves the water management in the cell, in particular at the cathodic site where water is the product of reaction [9, 22-23].

Usually, two layers constitute the GDM: a macroporous substrate made of carbon cloth or carbon paper called Gas Diffusion Layer (GDL) and a carbon-based coating called Microporous Layer (MPL). At first, the introduction of the GDL improved the performance and the efficiency of the cells. The application of the MPL resulted in a further optimization of the devices, in particular for what concerns the water management in conditions of high humidity [24-26].
PEMFCs feature a two-phase transport system that involves the gases fed to the cell, which contain both the reactive species and water vapour, and the liquid water obtained by the condensation of the vapour present in the gas flows or produced by the reaction at the cathode [27-29]. In addition, other phenomena that involve the electrolyte must be considered, as the electro-osmotic drag and the back diffusion [30-33]. The former generates a flow of water molecules from the anode to the cathode due to the applied potential across the MEA; the latter instead promotes the re-hydration of the anode due to progressive building up of both a concentration and a pressure gradient that pushes water back from the cathodic side. Normally, the first mechanism is much more intense, therefore the anodic side and the electrolyte experiences a gradual dehydration. Instead, back diffusion starts to influence the water balance in the

MEA when its accumulation at the cathodic side builds up significantly, that is at high current density. Whenever water saturates the GDM or the CL preventing the feeding of the required amount of gas to the reactive sites, the so-called "flooding" occurs and the cell potential drops due to mass transfer issues. This normally happens at high current densities, due to the need of larger amounts of reactants and the consequent high production of water. This mechanism prevents the PEMFC from being exploited at their maximum of power densities and solving this issue is challenging because multiple phenomena are involved and blockage of oxygen feeding can occur both inside the layers (CL, MPL or GDL) and at their interfaces [34].

A possible strategy that reduces the risk of water saturation is adopting a high working temperature in the cell that hinders condensation, i.e. the formation of the liquid phase responsible for the increase of mass transfer resistance [35]. This effect is particularly enhanced in structures featuring hydrophobic pores, where the vapour pressure of water is also increased as an effect of the radius according to the Kelvin equation (Eq. (1)):

$$\ln(P_{cur} / P_{flat}) = - 2 \gamma V_m / r R T \quad (1)$$

where P_{cur} is the effective vapour pressure on the curved surface, P_{flat} is the vapour pressure on the flat surface, γ is the surface tension at the liquid-vapour interface, V_m is the molar volume of the liquid, r is the radius of the meniscus of the liquid phase (that is affected by the pore radius and hydrophobicity), R is the gas constant and T is the temperature.

Moreover, high temperature also leads to other important advantages, such as higher diffusivity of the gases that promotes mass transfer, higher proton mobility in the electrolyte, higher exchange current density, larger tolerance for carbon monoxide and faster kinetics of reaction [36-39]. However, higher temperatures reduce the theoretical efficiency. In addition, they are also responsible for the dehydration of the electrolyte, which leads to loss of proton conductivity and large internal resistances, and for the increase of the transport coefficient, that enhances the activation losses.

In our work, we try to identify the main morphological and electrical MPL features that could contribute to an improvement of the cell performance at high temperature and reduced gas flows relative humidity. For this purpose, we have employed multiple type of carbon nanoparticles with different characteristic size, structure and properties in addition to carbon black (CB) [40], which has already been largely investigated [41-43]. In particular, we have focused on a series of graphene nanoparticles of different dimensions and properties because of their exceptional electrical and thermal conductivities, in addition to the promising improvements induced on MPL durability [44-49]. We have also studied the performances obtained with mixed composition featuring a carbon black-graphene nanoparticles weight

ratio of 1:1, aiming at detecting synergic effects between the two carbon phases. Currently, very limited efforts have been done in the direction of the substitution of carbon black with other materials for MPLs, in particular if graphene-based particles are considered [44-50].

2 EXPERIMENTAL METHODS

2.1 MPL MATERIALS AND PREPARATION

A 400 μm thick commercial carbon cloth, SCCCG5N by SAATI SpA, was employed as macroporous GDL. It underwent a series of pre-treatments aimed at increasing its hydrophobicity. First, a 15 minutes cleaning treatment by ultrasonic bath in acetone was performed, followed by a 5 minutes drying phase at 60 °C. Then, it was soaked in a 12 wt.% fluorinated ethylene propylene (FEP) solution by Chemours for 20 minutes (10 minutes per each side). Afterwards, it was heat-treated at 270 °C for 30 minutes to remove water and sinter the polymer uniformly on the carbon fibres [51].

Nine carbon-based inks were prepared by dispersing different combinations of carbon phases in a 55 wt.% FEP suspension, deionized water (DI) and isopropyl alcohol (IPA) as dispersing agent. The carbon phases employed in this work are:

- carbon black (CB), Vulcan XC72R by Cabot Italiana SpA;
- small size graphene nanoplatelets (GNP-S), by Sigma Aldrich;
- medium size graphene nanoplatelets (GNP-M), by Sigma Aldrich;
- exfoliated graphite (EG), PENTAGRAPH30 by Pentachem Srl;
- multi-wall carbon nanotubes (CNTs), NTX1 by Nanothinx.

The carbon phase was alternatively CB, GNP-S, GNP-M and EG alone or a combination of CB with alternatively GNP-S, GNP-M and EG in a 1:1 weight ratio. All the mixes featured a 10 wt.% addition of CNTs that has been proved to improve the conductivity of the MPL [52-53].

The inks were mechanically stirred at 8000 rpm by Ultra-Turrax T25 (IKA) for 15 minutes to achieve a homogeneous dispersion of the components. The GDLs were coated with these slurries by doctor-blade technique (K CONTROL COATER by RK PrintCoat Instruments Ltd), with a fixed gap of 440 μm between the blade and the plate in order to produce a 40 μm MPL coating. Then, the samples underwent a heat treatment at 270 °C for 30 minutes to remove water and IPA. Finally, the obtained GDMs were soaked once more into FEP suspension following the same procedure exploited for the GDLs in order to enhance the adhesion between MPLs and GDLs.

The produced GDMs featured a carbon loading of 2 mg cm^{-2}.

2.2 MICROSTRUCTURAL, MORPHOLOGICAL AND ELECTRICAL CHARACTERIZATION

To understand fully the influence of each carbon phase on the performance of the cell, both the particles alone and within the prepared MPLs were analysed.

MPL samples images were obtained by Scanning Electron Microscopy (Cambridge Stereoscan 360) and were used to determine the average size and the distribution pattern of particles, defects and pores. The image processing software ImageJ performed this analysis.

Investigation on the overall pore volume and the pore size distribution of the particles, the inks and the GDMs produced was performed by mercury intrusion porosimetry (MIP) by means of an Autopore V9600 by Micrometrics Instrument Corporation. From this analysis, we were also able to evaluate other parameters, such as bulk and skeletal densities, porosity and an estimation of the average pore size. The dimension of the pores intruded at the different pressures was calculated from the Washburn equation (Eq. (2)) [43]:

$$d = - (4 \gamma \cos\theta) / P \qquad (2)$$

where d is the pore diameter, γ is the mercury surface tension (485.5 mN m^{-1} at 298 K), θ is the contact angle between mercury and the pore walls (for Hg-GDM the value recorded is 130°) and P is the external pressure applied by the instrument.

The hydrophobicity of the MPLs surface has been evaluated through static contact angle analysis as an average of ten measurements obtained by sessile drop technique (OCA15Plus by DataPhysics Instruments). The analyses were performed on different areas of the MPL coatings to minimize the dependence on the local morphology of the surface, as the presence of large particle clusters, defects or cracks.

The particles were subjected to thermogravimetric analysis to get further information on their chemical composition that could be partially responsible for the final wettability of the coatings. The analysis were performed by DTA-TG SEIKO 6300 thermal analyser under flowing air in the temperature range 25 - 1000 °C with a heating rate of 10 °C min^{-1}.

A home-built system, similar to those described in Refs. [54-55], was exploited for measuring through-plane water permeability of the GDMs. A stainless steel filter holder (Millipore Instruments), which featured the MPL holder at its bottom, and a rigid transparent plastic tube to its upper part aiming to check the maximum water level corresponding to the breakthrough pressure, was used. Water was fed continuously from the upper opening of the tube until the first water droplets started to permeate through

the GDM, used as a filter. We calculated the hydrostatic head applied to the sample from the height of the water accumulated in the transparent cylinder. The pressure decrease was then related to both the water flow rate variation, measured as mass permeated per unit of area and time, and the permeability coefficient of the sample. This was calculated according to the Darcy's law, assuming a laminar flow through the membrane, as shown in Eq. (3):

$$K = (\Delta m\ \mu\ L) / (A\ \rho^2\ g\ \Delta h\ \Delta t) \quad (3)$$

where K is the permeability coefficient, Δm is the variation of mass of permeated water, μ is the viscosity of water at standard condition ($8.891\ 10^{-4}$ Pa s at 298 K), L and A are respectively the thickness and the surface area of the GDM in the orthogonal direction with respect to the water flow, ρ is the density of water, g is the gravitational acceleration, Δh is the variation of the water level height inside the system and Δt is the interval of time considered.

The value of K is given by the contribution of many factors, as the overall porosity, the pore size distribution, the presence of macro-cracks or defects, the thickness of the MPL, the tortuosity of the pore network and the hydrophobicity of the MPL material. Various attempts of distinguishing between the effects of all these features have been done in the past, from the description provided by the Carman-Kozeny equation to more specific models as the one proposed by Holzer et al. [56-57] However, these solutions usually fit specific samples and could not be adapted to all our MPLs without corrections that exceed the purpose of this study. For this reason, we adhered to the definition provided by the Darcy's law.

All the samples electrical resistances were assessed along both the through-plane and the in-plane directions. The former was measured by a home-built system aimed at reproducing the compressive action of the cell on the GDM that affects its bulk and contact resistance [58-62]. Indeed, we rearranged a fuel cell by placing its gold collectors on the inner sides of the bipolar plates in order to have them directly in contact with the samples, we removed the membrane electrode assembly and we connected the collectors to an external ohmmeter. The clamping force applied to this dummy cell was the same employed for the real operating cell. The values of resistivity were calculated from Eq. (4):

$$\rho_t = (R_t\ A) / L \quad (4)$$

where R_t is the resistance measured by the ohmmeter, A is the surface area of the sample and L is its thickness.

Instead, the in-plane electrical resistance was measured by placing the electrodes of the ohmmeter to the opposite side of stripes of the samples with a specific geometry. The in-plane resistivity (ρ_i) was evaluated through the Eq. (5):

$$\rho_i = (R_i A) / d = (R_i L h) / d \quad (5)$$

where R_I is the electrical resistance measured, A is the area crossed by the electron flux and d is the distance between the two test leads (i.e. 2.5 cm). In this case, the area is represented by the cross section of the GDM and thus, it is calculated as the sample thickness (L) times the sample height (h = 1 cm).

2.3 FUEL CELL PERFORMANCE TESTING

Single cell performances were investigated under four different operating conditions given by the combinations of two temperatures (60 °C and 80 °C) and two RHs (60 % and 100 %) of the gas flows at both the anodic and the cathodic side. The MEA (Baltic Fuel Cells GmbH) employed for all the testing sessions featured a Nafion 212 membrane as electrolyte coated at each side by catalyst layers, which had a 0.2 mg cm^{-2} and a 0.4 mg cm^{-2} platinum loading at the anode and cathode respectively. The gas flow rates were 0.25 NL min^{-1} and 1 NL min^{-1} for hydrogen and air respectively. Air and hydrogen were fed with stoichiometric ratios respectively equal to 2 and 1.2 at 30 A to enhance the water removal and to compensate for the concentration losses that are higher at the cathode. The cell potential values were recorded from the open circuit voltage (OCV) configuration up to the limiting current density with constant steps of 0.088 A cm^{-2}.

3 RESULTS

3.1 MORPHOLOGICAL AND MICROSTRUCTURAL CHARACTERISTICS

The SEM images reveal that the coatings are drastically different. The first main distinction can be made between the type of morphology generated by carbon black and that of graphene-based particles. Indeed, as already known from literature [63-64], carbon black consists of nano-size particles that tend to agglomerate due to Van der Waals interactions forming a sponge-like macro-structure with micropores. These have a diameter that ranges from 30 nm to 70 nm. As can be seen from Figure 1B, the coating seems to be quite homogeneous in terms of pore size. However, a large and continuous network of macro-cracks characterizes the whole surface of the sample (see Figure 1A). This mud-cracking phenomenon can be ascribed to the agglomeration mechanism, which induces the migration of isolated carbon particles toward denser areas and the formation of island-like structures, in particular during the thermal treatment phase of the samples preparation (see Section 2.1). Mud-cracking is typical of CB-based MPLs and, as described in literature, it is induced by shrinkage due to solvent evaporation during the final thermal treatment of the samples [65].

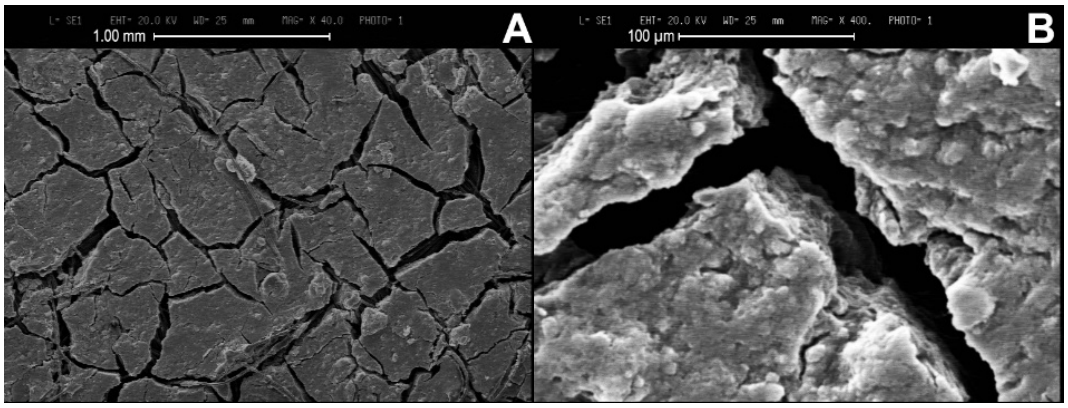

Figure 1: SEM images of the MPL surface of the CB sample obtained with magnification: A) 40x; B) 400x.

Figure 2 shows that all the graphene-based particles have larger characteristic sizes compared to carbon black. The average particle dimensions are 5 µm, 25 µm and 500 µm for GNP-S, GNP-M and EG respectively. Similarly, the observed average pore size of the coatings increases with the dimension of the carbon phase: smaller particles tend to pack more densely, thus leaving reduced interstitial voids [47-48]. In addition, it is important to notice from Figure 2C and 2E that GNP-S features the same agglomerating tendency as CB, which leads to mud-cracking on its surface. Although these cracks can be detected easily, their size is not comparable with those of CB and there is no certainty about whether they reach the GDL at their bottom or they are sealed with GNP-S particles. These defects are completely absent in both GNP-M and EG (see Figure 2A, 2B, 2D and 2E), suggesting that this phenomenon has an effect on the coating only if the particle size is below 10 µm.

From GNP-S to EG it can also be observed that the larger the particles, the higher their probability of being placed in a parallel direction with respect to the substrate. Indeed, EG particles are stacked more regularly than any other sample. This could be likely due to the sedimentation of the particles in the liquid phase of the slurries and to the mechanical action of the blade during doctor-blade coating procedure: the larger the surface of the carbon phase, the higher the probability of applying a momentum to the particles, thus rotating them in parallel with the sliding direction of the blade.

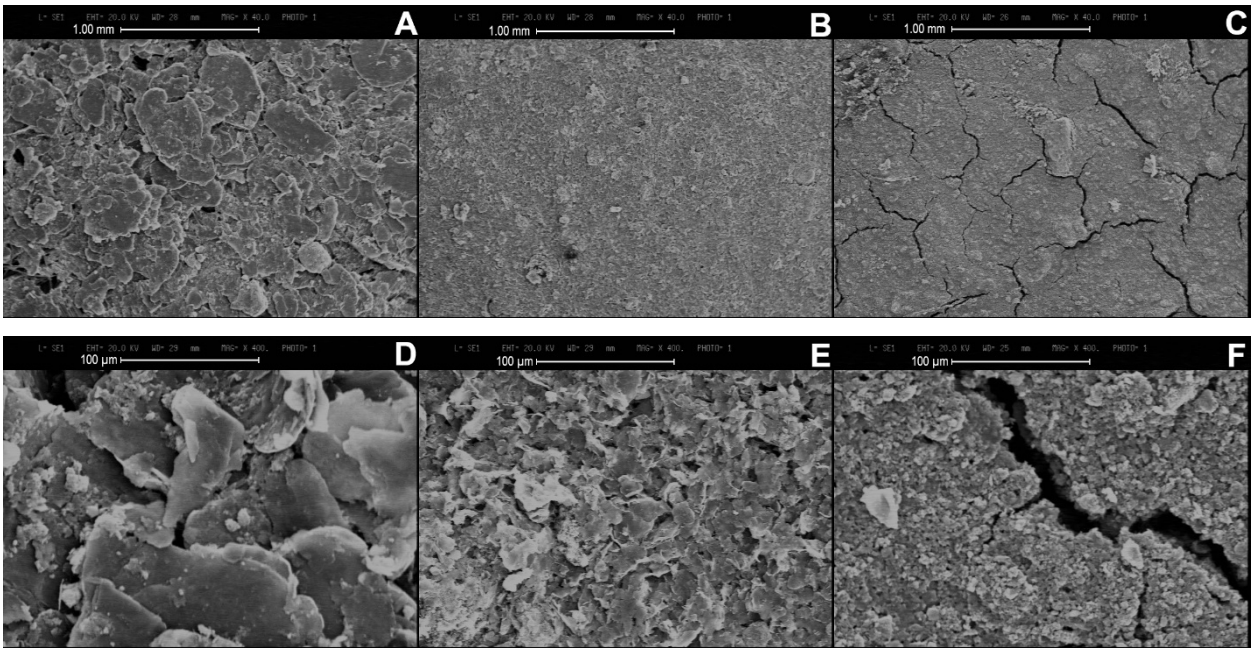

Figure 2: SEM images of the MPL surface of the graphene samples: A) EG 40x; B) GNP-M 40x; C) GNP-S 40x; D) EG 400x; E) GNP-M 400x; F) GNP-S 400x.

Regarding the mix compositions samples, SEM images show that the CB tends to deposit on the flat surface of the graphene-based particles forming the usual agglomerates characterized by micropores. In the case of EG (see Figure 3A and 3D), CB seems to form a cracked coating on top of the EG-based layer because it has large flat surfaces on which the agglomerates can be easily accommodated. By reducing the particle size, as for CB_GNP-M in Figure 3B and 3E, the agglomeration of CB is limited by the less regular disposition of the graphene particles and consequently the cracking mechanism is hindered. However, excessively small dimensions, as those of GNP-S, promote a more homogeneous dispersion of the different carbon phases with less defined distinctions between them. The deposition of this type of slurries produces coatings that feature large cracks in between the CB islands and GNP-S-induced smaller cracks inside these islands (see Figure 3C and 3F).

SEM images also allow evaluating the roughness of the MPL surfaces under a qualitative point of view. It is evident that the increase of the particle size affects negatively the smoothness and regularity of the surface, as for the case of EG that features a terrace-like aspect [44]. The addition of CB produces a filling effect that reduces the depth of the surface valleys, even though it introduces also cracks that hinder the homogeneity of the MPL. Considering these features is fundamental because they have an

impact on all the phenomena involving the interface between the MPL and the CL, such as the electrical and the thermal conductivities and the water management.

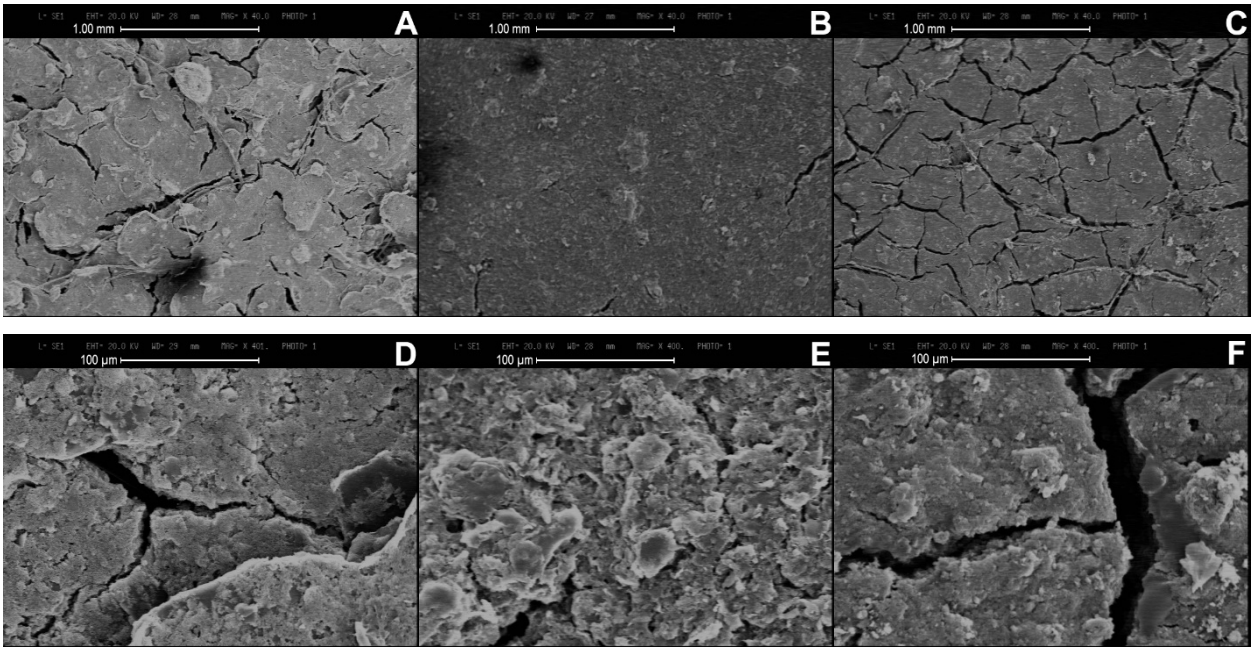

Figure 3: SEM images of the MPL surface of the graphene samples: A) CB_EG 40x; B) CB_GNP-M 40x; C) CB_GNP-S 40x; D) CB_EG 400x; E) CB_GNP-M 400x; F) CB_GNP-S 400x.

Most of the first evaluation of the porosity of the samples provided by the SEM analysis are confirmed by mercury intrusion porosimetry. First, the distinction between different size pores is based on the diffusion mechanism of the gas inside them. Knudsen diffusion occurs in pores with a dimension similar to the gas mean free path ($\lambda_{air} \approx 70$ nm), instead bulk diffusion is featured in pores whose size is about one hundred times larger [10]. Mixed diffusion mechanisms are typical of intermediate size pores. Therefore, we will distinguish between micropores with $d < 0.07$ µm, macropores with $d > 7$ µm and mesopores with 0.07 µm $< d < 7$ µm.

From Figure 4A, it is possible to observe that CB-based GDM features a larger cumulative volume compared to the other samples and a specific bimodal pore distribution (see Figure 4B) [46]. This is given by the presence of the micropores inside the agglomerates with a diameter of 30 - 70 nm and the presence of cracks with dimension of 70 - 90 µm, whose volume corresponds to that of the GDL pores. Since the cumulative volume of the GDM with CB is larger than that of the GDL alone, it can be asserted that either the CB penetration in the GDL is very limited or the cracks volume is so large that it compensates for the reduction of GDL pores volume due to CB penetration.

The graphene-based MPLs behaviour varies drastically depending on the sample considered. EG and GNP-S porosities give similar results both in terms of cumulative volume and size distribution, however the pore features are different. Indeed, EG features densely stacked large particles that produce a dense coating on top of the GDL with macropores of 30 - 60 μm of diameter. The penetration of the particles in the GDL is very limited as suggested by the minimal variation of the cumulative volume curve in the region of $d > 80$ μm: this is reasonable considering that the average size of the EG particles is larger than most of the GDL macropores. In the case of GNP-S, the coating microstructure is different. In this case, the macroporosity contribution is attributed to the presence of cracks, which are smaller with respect to those of CB and correspond to the porosimetry peaks in between 40 μm and 60 μm. The pore size distribution curve seems to suggest that the ink has a limited penetration in the GDL likely due to the formation of wide clusters of particles with a larger characteristic size than the GDL voids. Instead, the pores inside the agglomerates are smaller (0.3 - 4 μm) and their contribution is limited in terms of cumulative volume. Finally, GNP-M behaviour can be drastically distinguished from the previous ones. Indeed, a huge reduction of volume in the region of $d > 10$ μm can be noticed most likely due to the penetration of individual particles inside the GDL cloth [43]. These results confirms that GNP-M does not form large clusters as GNP-S, as previously asserted. A drastic growth of the cumulative volume occurs for $d < 10$ μm, which is compatible with the pore size observed via SEM analysis.

The addition of CB has different effects on the porosities of the samples, as can be seen in Figure 4C and 4D, due to the distinguished interactions it has with the three different kinds of particles. As already observed, CB tends to form a thick and homogeneous layer on top of the EG particles with just a little penetration in between them and this is confirmed by the pore size distribution curve. Indeed, this features two new peaks corresponding to the introduction of cracks (macroporous region) and the introduction of micropores and a reduction of volume in the 30 - 60 μm diameter region. A similar behaviour can be observed also for CB_GNP-M, but a much more significant decrease is detected in the mesoporous region due to CB filling and less micropores are present due to reduced CB clusters size in between the graphene particles. Finally, CB_GNP-S is the only sample experiencing a consistent increase of micropores and a sharp decrease of macropores. The increase of the pores with $d < 1$ μm can be explained as the combination of the agglomeration tendencies of both particles that leads to the formation of a mixed structure with pores in between CB particles alone, GNP-S particles alone and in between the two of them. On the contrary, the decrease in the macroporous area is difficult to be justified because of the spread of large cracks on top of the MPL. The only possible explanation is a consistent penetration of particles inside the GDL that compensate for the crack formation. This could be due to the fact that in

the liquid phase of the slurry the mixed clusters could be reduced in dimension, thus facilitating the filling of the carbon cloth pores during the subsequent coating process.

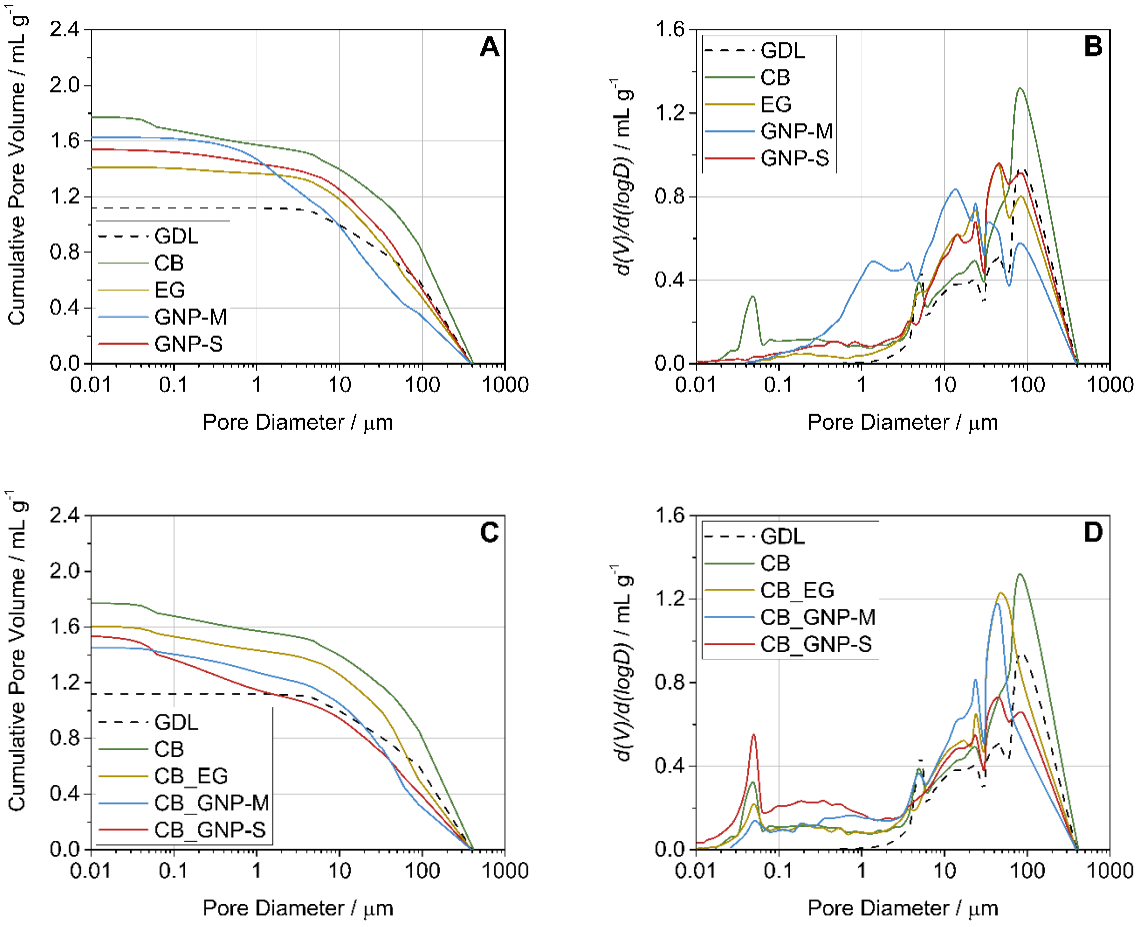

Figure 4: (A) Cumulative pore volume and (B) pore size distribution curves of the monocomponent samples. (C) Cumulative pore volume and (D) pore size distribution curves of the multicomponent samples.

The physical properties analysed by SEM and MIP seem to have a minor effect on the wettability of the surfaces. From Table 1, it is possible to observe that all samples are super-hydrophobic with the exception of the EG-based MPL surface. Therefore, it is safe to assume that the major contribution to the samples hydrophobicity is given by the fluorinated coating obtained by immersion of the GDM in the 12 wt.% FEP suspension. There seems to be a possible minor relation between the pores dimension and the static contact angle (SCA) measurement, according to the Young-Laplace equation (see Eq. (6)): larger pores, as those of EG, generate a reduced capillary pressure, therefore a limited repulsive effect on the water droplet that limits the contact angle with the MPL surface, and vice versa.

$$P_c = 2\,\gamma\cos\theta / r \qquad (6)$$

In Eq. (4) P_c is the capillary pressure, γ is the surface tension at the water-air interface, θ is the droplet contact angle and r is the pore radius.

Table 1: Static contact angle measurements of the MPLs produced.

	CB	**EG**	**GNP-S**	**GNP-M**	**CB_EG**	**CB_GNP-S**	**CB_GNP-M**
SCA / °	151.9	146.7	161.9	157.3	155.4	150.4	156.1

Thermogravimetric analyses (see Figure 5) of the particles seem to exclude distinctions in their composition that could justify the different degrees of surface wettability. The results are shown from room temperature up to 500 °C because this range of analysis is sufficient to highlight the possible presence of moisture and oxygenated groups that could be responsible for a diminished hydrophobicity. EG has a higher level of initial hydration; however, GNP-M features larger losses in the 150 - 350 °C that could be due to a slightly more significant presence of oxygenated groups. This could be due to a lateral surface with more defects, which promote the formation of chemical bonds with oxygen, of this nanoplatelet with respect to GNP-S and due to a much higher specific area compared to EG. Anyway, the presence of oxygen atoms seems to be overcome by the effect of the surface morphological properties.

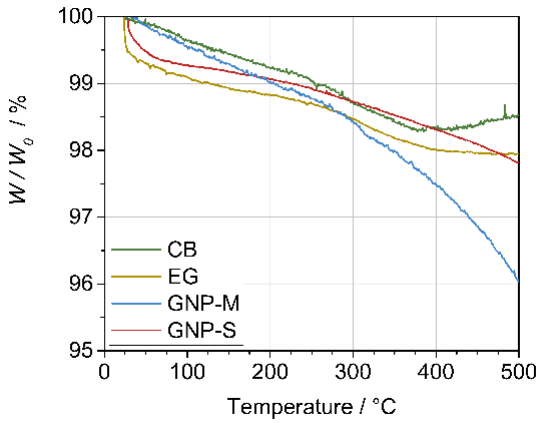

Figure 5: Thermogravimetric analysis of the carbon particles used in this study.

The water permeability measurements show that the samples have drastically different behaviours (see Figure 6A). Indeed the breakthrough pressures for CB and EG are low and are equal to 1133 Pa and 1189

Pa respectively. In the first case, water is able to penetrate easily through the MPL because of the wide macro-cracks spread on the whole surface of the sample [66]. It is safe to assume that water reaches directly the GDL at the cracks floor; otherwise, the assessed pressure value would be much higher because of the limited liquid penetration in the hydrophobic micropores. The case of EG is different because of its morphology. The MPL is not cracked, however it features large holes (see Figure 1) that facilitate the passage of water. The rest of the macropores are placed mainly longitudinally, which could decrease the permeability resulting in a higher tortuosity of the path; however, their size is large enough to allow the fast infiltration of water. The water flux is slightly larger for EG, probably because the penetration occurs on the whole surface of the sample, not only in correspondence of the cracks. An interesting aspect is the increase of permeability of these samples during the measurements: in both cases, this evolution is due to the gradual degradation of the MPL that opens up new path for the water flows (see Figure 6B).

For GNP-S and GNP-M the breakthrough pressures are much higher (4581 Pa and 7220 Pa, respectively) and the values of permeability are almost two orders of magnitude less than those of EG and CB. This weak permeability is the result of three factors: the smaller average diameter of the pores with respect to EG, the high packing density of the particles and the reduced presence of cracks (GNP-S) or their complete absence (GNP-M) [48]. Consequently, the water flux has to split into small droplets to infiltrate in the MPL and their path is slowed down by the tortuosity of the pore network.

As could be easily predicted, the addition of CB promotes the mud-cracking of the surface that has a detrimental effect on the breakthrough pressures of GNP-S and GNP-M that decrease of – 11.57 % and – 31.39 % respectively and on the permeability that increases of almost an order of magnitude for both samples (see Figure 6C and 6D) [45]. However, these values are still lower than those registered for CB alone.

On the contrary, EG features a drastic increase of the breakthrough pressure (+ 140.12 %) but a higher permeability. The increase of pressure could be due to the occlusion of the pores by CB particles that leaves less open path for water to infiltrate. The higher permeability can be explained in the same manner: water cannot easily penetrate through the pores because of their reduced radius, which means that the flux is concentrated near the cracks. Once the hydrostatic head has opened the path in the cracks, water can flow directly into the GDL.

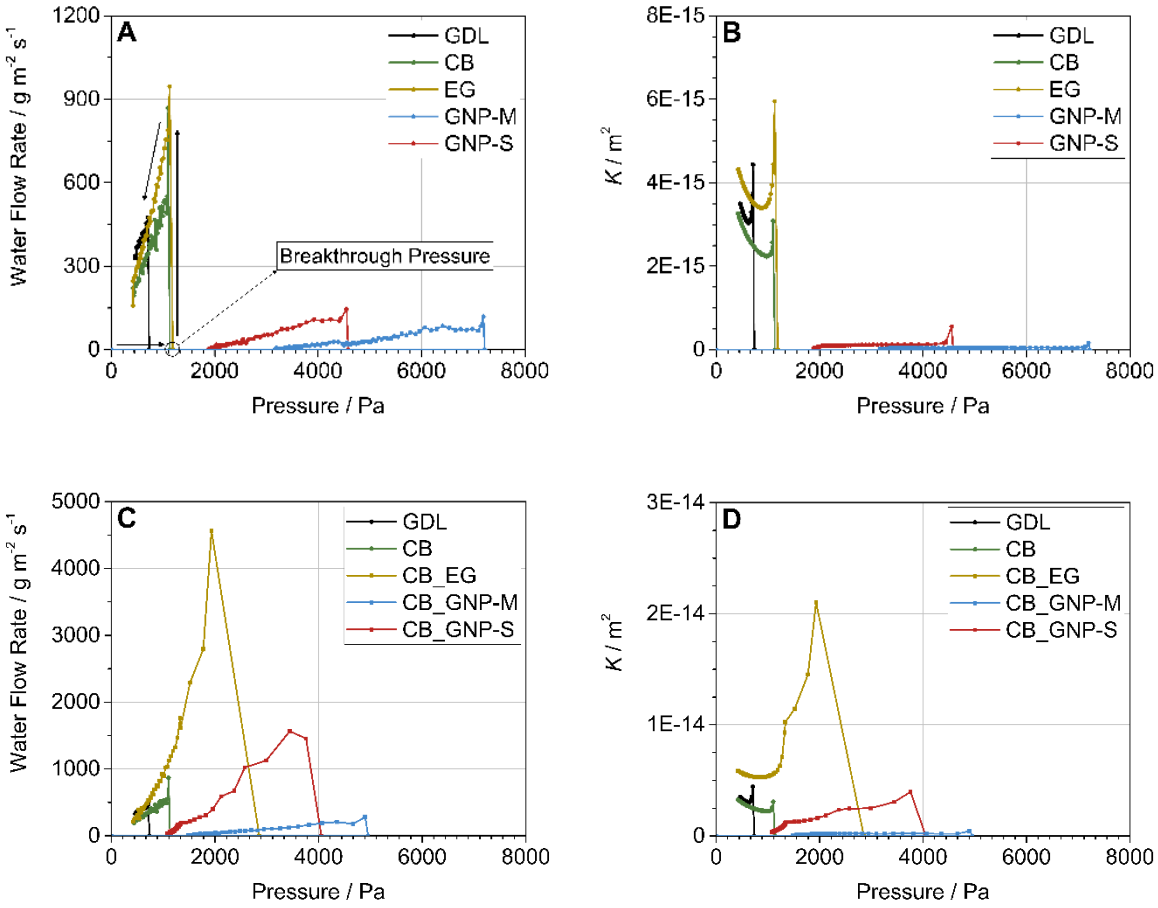

Figure 6: (A) Water flow rate and (B) permeability coefficient curves of the monocomponent samples. (C) Water flow rate and (D) permeability coefficient curves of the multicomponent samples.

3.2 ELECTRICAL CHARACTERIZATION

The measured electrical resistances (see Table 2 and 3) reveal that the presence of CB in the MPL has two opposite effects along the in-plane and the through-plane directions. First, it is important to notice that single-particle graphene has an exceptional in-plane conductivity, which experiences a dramatic reduction of about six orders of magnitude in bulk powders, although it still remains higher than that of CB [67]. The values of in-plane resistivity show that small differences exist between the samples with graphene-based particles. GNP-M features the lowest value probably due to the absence of cracks, which would affect positively the electrical continuity of the MPL [44]. In the transverse direction, the resistivity values are higher than those in the longitudinal direction because GDL and MPL act like in-series resistances. The reduction of porosity of the samples upon compression partially compensate for the higher resistivity of the GDL. The through-plane resistances are still lower for the graphene-based

samples than the CB, but the addition of this carbon phase is beneficial. This is probably due to the isotropic character of CB conductivity and its tendency to occlude the pores between the stacked nanoplatelets, thus increasing the available electrons path [45, 48]. EG features the lower resistances of the pure samples, accordingly with the results of Marinho et al. [67].

Table 2: In-plane resistivity values of the GDMs produced.

In-plane	Resistance [Ω]	Thickness [µm]	Resistivity [mΩ cm]
CB	2.28	450	41.04
EG	1.45	470	27.26
CB_EG	1.49	460	27.42
GNP-S	1.43	430	24.60
CB_GNP-S	1.32	510	26.93
GNP-M	1.29	470	24.25
CB_GNP-M	1.46	435	25.40

Table 3: Through-plane resistivity values of the GDMs produced.

Through-plane	Resistance [mΩ]	Thickness [µm]	Resistivity [mΩ cm]
CB	0.4392	255	155.01
EG	0.2541	270	84.70
CB_EG	0.2425	300	72.75
GNP-S	0.3632	290	112.72
CB_GNP-S	0.2452	320	68.96
GNP-M	0.3989	250	143.60
CB_GNP-M	0.2358	300	70.74
GDL	0.2068	230	80.92

3.3 SINGLE CELL PERFORMANCE

Single cell testing has been performed under four different conditions that span from a highly humid to a highly dry environment. Specifically, we should expect water saturation-related issues at 60 °C with

RH = 100% and dehydration problems at 80°C and RH = 60 %. This procedure allows us to better assess which mechanisms and phenomena related to the water management are predominant in the cell and to identify possible corrections in the manufacturing process of the MPLs.

From the graphs in Figure 7, CB appears to be the overall best performing sample in terms of peak power densities achieved. This is due to the fact that the cell keeps working at high current densities and it has the lowest mass transfer resistances out of the four samples under all conditions but T = 80 °C and RH = 100 % (see Figure 7D). This is probably due to the presence of both micropores, which enhances the water removal from the MPL due to the effect of the gradient of capillary pressure, and cracks, which allow the fast diffusion of oxygen toward the catalyst layer under critical conditions [9, 43]. At both low and high temperature, the increase of relative humidity of the flows is detrimental in terms of mass transfer because it accelerates the condensation of water, thus inducing the flooding of the cell at an earlier stage. However, the large gas permeability due to the macrocracks presence is also responsible for the enhanced dehydration of the MEA under low humidity conditions. This induces an increase of the ohmic resistance because of the reduced proton conductivity of the Nafion membrane employed.

The EG sample has the worst performances out of all the MPLs under all sets of conditions. At low temperature, the cell performs well at low-medium current densities. However, as soon as the current starts increasing, the cell experiences a sharp voltage drop related to the flooding of the cell, as can be seen from Figure 7A. Seemingly, the water produced at the CL tends to accumulate in the longitudinal pores of the MPL due to their tortuosity and large size and, as the vapour pressure increases, the water condensates in the MPL and the oxygen diffusion is hindered. In addition, water films could form at the interfacial voids between the CL and MPL due to its high roughness [34, 68-69]. The low slope of the polarization curve at high current density, which may be ascribed to low mass transfer resistance due to limited condensation at high temperature, confirms this. However, working at 80 °C is not beneficial either because the excessive dehydration of the electrolyte prevents the proper functioning of the cell.

The GNP-S allows maintaining optimal membrane hydration under all sets of conditions, probably due to the low gas permeability of the sample. This also suggests that the small cracks on its surface have a minimal impact on the performance. However, the mass transfer is once more critical with little improvement at T = 60 °C - RH = 100 % (Figure 8B) and T = 80 °C - RH = 60% (Figure 7C).

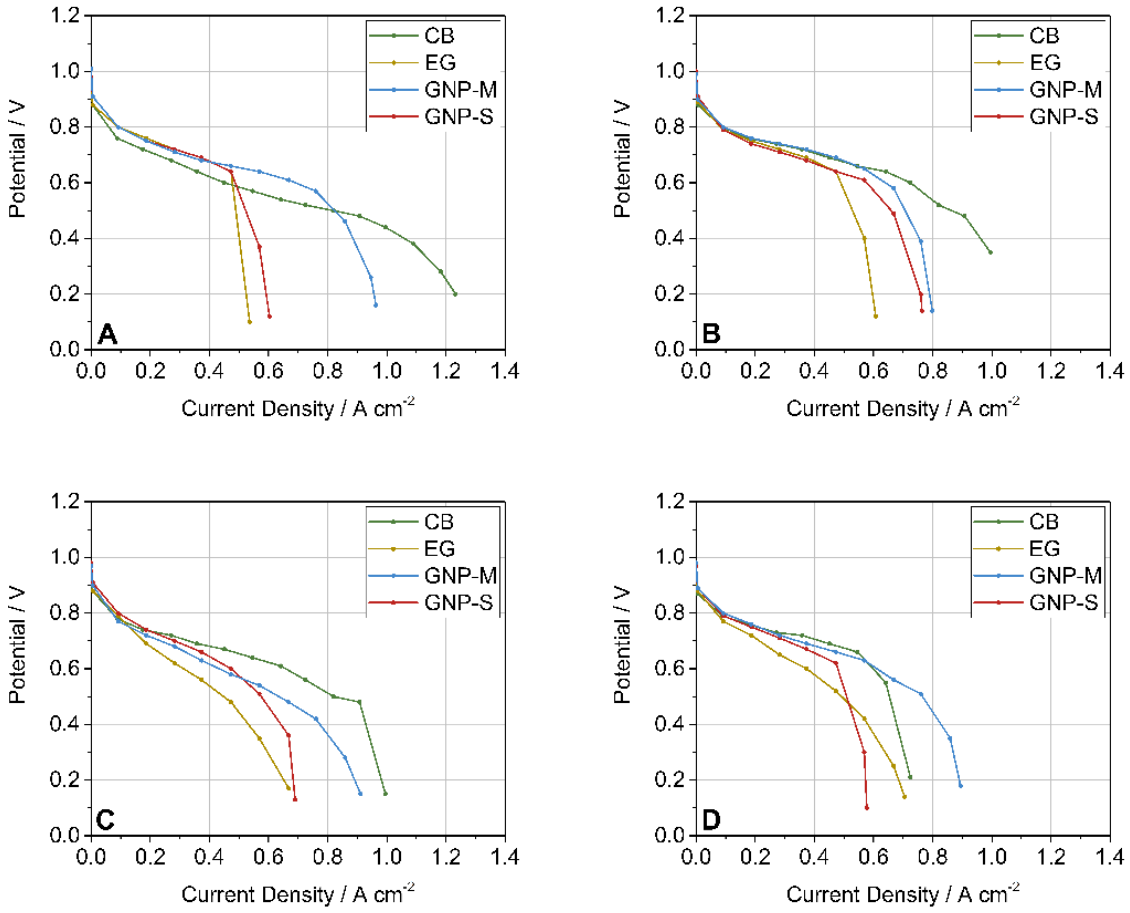

Figure 7: Polarization curves of the monocomponent samples obtained under the following conditions: A) T = 60 °C and RH = 60 %; B) T = 60 °C and RH = 100 %; C) T = 80 °C and RH = 60 %; D) T = 80 °C and RH = 100 %.

These two sets of conditions are opposite in terms of humidity, which is controversial. Surely, the dry environment hinders the condensation of water, thus improving the oxygen mass transfer. The lower mass transfer resistance at T = 60 °C - RH = 100 % can be explained only assuming that the MPL works properly because this is the first tested condition and the sample does not feature additional defects. The large detachments of fragments of the coating after the disassembling of the cell seems to confirm the extreme weakness of this sample, which could progressively compromise the performance of the cell. Finally, GNP-M is the best graphene-based sample, in particular if we consider the intermediate humidity conditions (T = 60 °C – RH = 60 % and T = 80 °C – RH = 100%). At T = 60 °C – RH = 100 %, the high humidity helps keeping the electrolyte hydrated, as the low ohmic losses suggest; however, the flooding is accelerated because the MPL has neither micropores to enhance water removal by capillary pressure

or large pathways, as cracks, that favour the bulk diffusion of oxygen [47-49]. At T = 80 °C – RH = 60 %, the condensation of water at high current density is limited, however the dehydration of the electrolyte is increased due to meso- and macro-pores that favour the diffusion of water vapour from the cathodic site toward the bipolar plate.

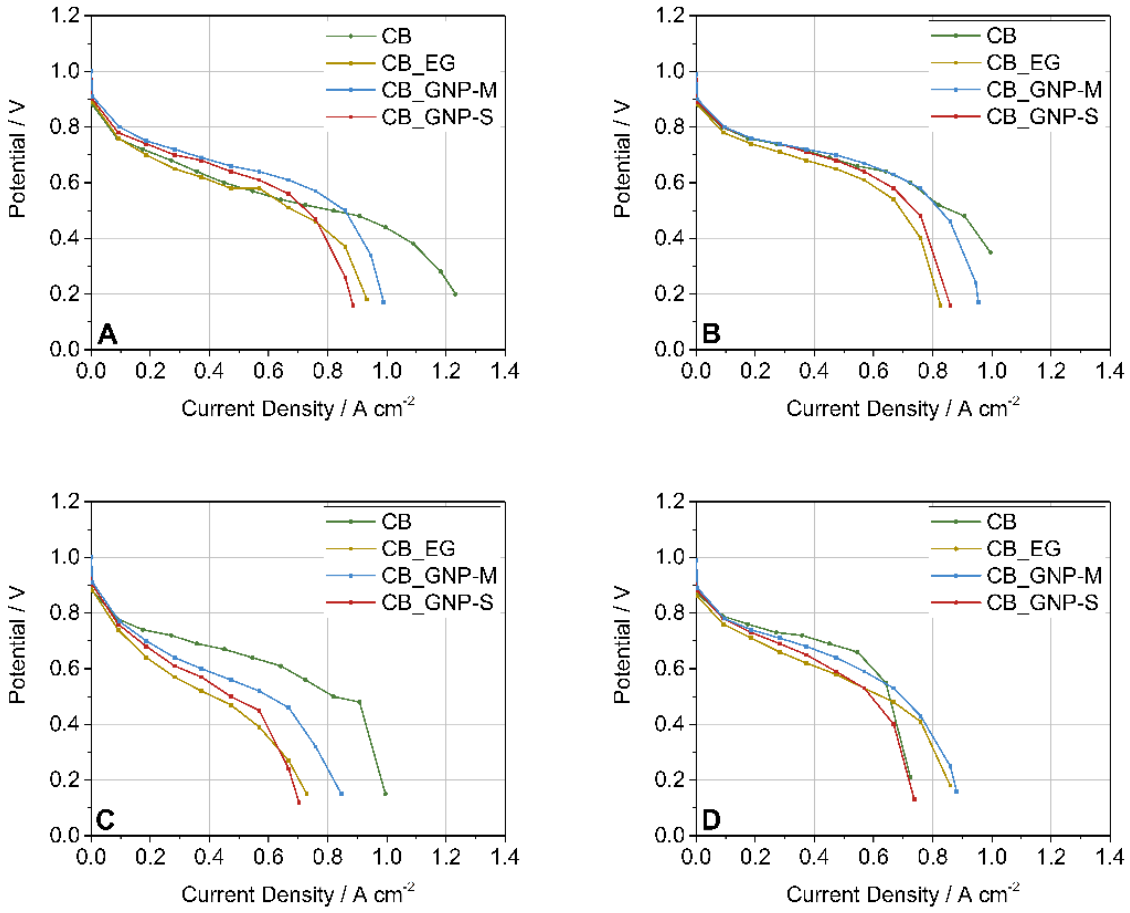

Figure 8: Polarization curves of the monocomponent samples obtained under the following conditions: A) T = 60 °C and RH = 60 %; B) T = 60 °C and RH = 100 %; C) T = 80 °C and RH = 60 %; D) T = 80 °C and RH = 100 %.

The addition of CB to these samples seems to have always the same effects, as can be seen from the graphs in Figure 8. The introduction of cracks hugely affects the capability of the MPLs of sealing the water close to the MEA, thus increasing its dehydration at 80 °C (see Figure 8C and 8D). At 60 °C this phenomenon is less relevant and ohmic losses are reduced thanks to the improved electrical through-plane conductivity of the samples. At high current density, a multitude of aspects should be considered,

however an overall improvement is evident. Surely, the introduction of micropores helps accelerating the ejection of water from the MPL and the introduction of cracks enhances the bulk diffusion of oxygen toward the CL. The filling of the large longitudinal pores reduces the risk of MPL occlusion by water condensation. Finally, the roughness reduction should avoid the formation of voids at the CL – MPL interface.

4 CONCLUSIONS

The employment of graphene nanoplatelets for the MPL has given promising results, but further improvements are needed. Comparing the samples obtained from different particles and mixed compositions has allowed identifying some of the main factors affecting the performance under different combinations of temperature and humidity:

- Cracks or large holes act as direct air paths that might improve the bulk diffusion when large amounts of oxygen are needed for the cathodic reaction; however, they hinder the durability of the coating, reduce the in-plane electrical conductivity and increase the MEA dehydration due to higher outward water diffusion.
- The specific packing behaviour of the graphene nanoplatelets might lead to the presence of longitudinal meso- and macro- pores, which increases the water retention by the MPL. This could compensate for the dehydration at high temperature, while enhancing the gas diffusion with respect to a microporous coating; however, it also increases the tortuosity of the pore network thus promoting flooding.
- The presence of micropores is beneficial as it reduces the accumulation of water in the MPL at high current density; however, the carbon black agglomerates responsible for them tend to reduce the gas permeability of the coating.

Both excessively small graphene nanoparticles and large exfoliated graphite cannot prevent mass transfer resistance increase at medium-high current densities. In the first case, the pores are too small to allow a sufficient diffusion of oxygen (in absence of large cracks); in the second case, the pores are so large that water easily permeates at low-medium current density and it tends to condensate inside them at high current density because of the extremely low capillary pressure that hinders its expulsion. Finding a compromise in terms of nanoplatelets size seems to be a viable solution to properly tune the porosity of the microporous layer, in order to obtain low ohmic and mass transfer voltage losses under low humidity condition.

REFERENCES

[1] G. V. Research, **2018**, p. 125.
[2] B. Spasova, D. Kawamoto, Y. Takefuji, *Energies* **2019**, *12*.
[3] J. Kast, G. Morrison, J. J. Gangloff, R. Vijayagopal, J. Marcinkoski, *Res Transp Econ* **2018**, *70*, 139-147.
[4] Z. P. Cano, D. Banham, S. Y. Ye, A. Hintennach, J. Lu, M. Fowler, Z. W. Chen, *Nat Energy* **2018**, *3*, 279-289.
[5] M. Wei, S. J. Smith, M. D. Sohn, *Appl Energ* **2017**, *191*, 346-357.
[6] S. Abuzant, S. Jemei, D. Hissel, L. Boulon, K. Agbousso, F. Gustin, *2017 Ieee Vehicle Power and Propulsion Conference (Vppc)* **2017**.
[7] Y. Wang, D. F. Ruiz Diaz, K. S. Chen, Z. Wang, X. C. Adroher, *Mater Today* **2019**.
[8] BP, BP Energy Outlook: 2019 edition, **2019**.
[9] J. H. Nam, M. Kaviany, *Int J Heat Mass Tran* **2003**, *46*, 4595-4611.
[10] M. V. Williams, E. Begg, L. Bonville, H. R. Kunz, J. M. Fenton, *J Electrochem Soc* **2004**, *151*, A1173-A1180.
[11] P. R. Chowdhury, A. Vikram, R. K. Phillips, M. Hoorfar, *J Power Sources* **2016**, *320*, 222-230.
[12] H. Sadeghifar, N. Djilali, M. Bahrami, *J Power Sources* **2014**, *248*, 632-641.
[13] N. Zamel, E. Litovsky, S. Shakhshir, X. G. Li, J. Kleiman, *Appl Energ* **2011**, *88*, 3042-3050.
[14] N. Zamel, E. Litovsky, X. G. Li, J. Kleiman, *Int J Hydrogen Energ* **2011**, *36*, 12618-12625.
[15] G. Unsworth, N. Zamel, X. G. Li, *Int J Hydrogen Energ* **2012**, *37*, 5161-5169.
[16] N. Zamel, X. G. Li, J. Shen, *Appl Energ* **2012**, *93*, 39-44.
[17] N. Zamel, J. Becker, A. Wiegmann, *J Power Sources* **2012**, *207*, 70-80.
[18] H. Pourrahmani, M. Moghimi, M. Siavashi, *Int J Hydrogen Energ* **2019**, *44*, 3121-3137.
[19] H. Sadeghifar, N. Djilali, M. Bahrami, *J Power Sources* **2015**, *273*, 96-104.
[20] H. Pourrahmani, M. Siavashi, M. Moghimi, *Energy* **2019**, *182*, 443-459.
[21] H. Pourrahmani, M. Moghimi, M. Siavashi, M. Shirbani, *Appl Therm Eng* **2019**, *150*, 433-444.
[22] J. Chen, T. Matsuura, M. Hori, *J Power Sources* **2004**, *131*, 155-161.
[23] E. Nishiyama, M. Hara, T. Murahashi, K. Nakao, *J Fuel Cell Sci Tech* **2015**, *12*, 051005-051005-051007.
[24] Z. G. Qi, A. Kaufman, *J Power Sources* **2002**, *109*, 38-46.
[25] A. Z. Weber, J. Newman, *J Electrochem Soc* **2005**, *152*, A677-A688.
[26] S. Park, J. W. Lee, B. N. Popov, *J Power Sources* **2006**, *163*, 357-363.
[27] M. Fazeli, J. Hinebaugh, Z. Fishman, C. Totzke, W. Lehnert, I. Manke, A. Bazylak, *J Power Sources* **2016**, *335*, 162-171.
[28] J. M. LaManna, S. G. Kandlikar, *Int J Hydrogen Energ* **2011**, *36*, 5021-5029.
[29] N. Zamel, X. G. Li, *Prog Energ Combust* **2013**, *39*, 111-146.
[30] W. Dai, H. J. Wang, X. Z. Yuan, J. J. Martin, D. J. Yang, J. L. Qiao, J. X. Ma, *Int J Hydrogen Energ* **2009**, *34*, 9461-9478.
[31] P. W. Majsztrik, M. B. Satterfield, A. B. Bocarsly, J. B. Benziger, *J Membrane Sci* **2007**, *301*, 93-106.
[32] Y. H. Park, J. A. Caton, *Int J Hydrogen Energ* **2008**, *33*, 7513-7520.
[33] F. N. Xu, S. Leclerc, D. Stemmelen, J. C. Perrin, A. Retournard, D. Canet, *J Membrane Sci* **2017**, *536*, 116-122.
[34] C. Simon, F. Hasche, H. A. Gasteiger, *J Electrochem Soc* **2017**, *164*, F591-F599.
[35] O. S. Ijaodola, Z. El- Hassan, E. Ogungbemi, F. N. Khatib, T. Wilberforce, J. Thompson, A. G. Olabi, *Energy* **2019**, *179*, 246-267.

[36] J. L. Zhang, Z. Xie, J. J. Zhang, Y. H. Tanga, C. J. Song, T. Navessin, Z. Q. Shi, D. T. Song, H. J. Wang, D. P. Wilkinson, Z. S. Liu, S. Holdcroft, *J Power Sources* **2006**, *160*, 872-891.
[37] K. Oh, H. Ju, *Int J Hydrogen Energ* **2015**, *40*, 7743-7753.
[38] P. Mocoteguy, B. Ludwig, J. Scholta, R. Barrera, S. Ginocchio, *Fuel Cells* **2009**, *9*, 325-348.
[39] A. Chandan, M. Hattenberger, A. El-Kharouf, S. F. Du, A. Dhir, V. Self, B. G. Pollet, A. Ingram, W. Bujalski, *J Power Sources* **2013**, *231*, 264-278.
[40] A. Asthana, T. Maitra, R. Buchel, M. K. Tiwari, D. Poulikakos, *Acs Appl Mater Inter* **2014**, *6*, 8859-8867.
[41] X. L. Wang, H. M. Zhang, J. L. Zhang, H. F. Xu, Z. Q. Tian, J. Chen, H. X. Zhong, Y. M. Liang, B. L. Yi, *Electrochimica Acta* **2006**, *51*, 4909-4915.
[42] M. J. Lázaro, L. Calvillo, V. Celorrio, J. Pardo, S. Perathoner, R. Moliner, *Study and application of carbon black vulcan XC-72R in polymeric electrolyte fuel cells*, **2011**.
[43] C. Simon, D. Kartouzian, D. Muller, F. Wilhelm, H. A. Gasteiger, *J Electrochem Soc* **2017**, *164*, F1697-F1711.
[44] M. J. Leeuwner, D. P. Wilkinson, E. L. Gyenge, *Fuel Cells* **2015**, *15*, 790-801.
[45] A. T. Najafabadi, M. J. Leeuwner, D. P. Wilkinson, E. L. Gyenge, *ChemSusChem* **2016**, *9*, 1689-1697.
[46] A. Ozden, S. Shahgaldi, X. G. Li, F. Hamdullahpur, *Renew Energ* **2018**, *126*, 485-494.
[47] A. Ozden, S. Shahgaldi, J. Zhao, X. G. Li, F. Hamdullahpur, *Fuel* **2018**, *215*, 726-734.
[48] M. J. Leeuwner, A. Patra, D. P. Wilkinson, E. L. Gyenge, *J Power Sources* **2019**, *423*, 192-202.
[49] S. Shahgaldi, A. Ozden, X. Li, F. Hamdullahpur, *Electrochimica Acta* **2019**, *299*, 809-819.
[50] M. Mariani, S. Latorrata, P. G. Stampino, G. Dotelli, *Fuel Cells* **2019**.
[51] S. Latorrata, R. Balzarotti, P. G. Stampino, C. Cristiani, G. Dotelli, M. Guilizzoni, *Prog Org Coat* **2015**, *78*, 517-525.
[52] S. Latorrata, P. G. Stampino, C. Cristiani, G. Dotelli, *Chem Engineer Trans* **2014**, *41*, 241-246.
[53] S. Latorrata, P. G. Stampino, C. Cristiani, G. Dotelli, *Int J Hydrogen Energ* **2015**, *40*, 14596-14608.
[54] J. H. Chun, K. T. Park, D. H. Jo, J. Y. Lee, S. G. Kim, S. H. Park, E. S. Lee, J. Y. Jyoung, S. H. Kim, *Int J Hydrogen Energ* **2011**, *36*, 8422-8428.
[55] J. Benziger, J. Nehlsen, D. Blackwell, T. Brennan, J. Itescu, *J Membrane Sci* **2005**, *261*, 98-106.
[56] P. C. Carman, *Chem Eng Res Des* **1997**, *75*, S32-S48.
[57] L. Holzer, O. Pecho, J. Schumacher, P. Marmet, O. Stenzel, F. N. Buchi, A. Lamibrac, B. Munch, *Electrochimica Acta* **2017**, *227*, 419-434.
[58] W. K. Lee, C. H. Ho, J. W. Van Zee, M. Murthy, *J Power Sources* **1999**, *84*, 45-51.
[59] D. K. Qiu, H. Janssen, L. F. Peng, P. Irmscher, X. M. Lai, W. Lehnert, *Appl Energ* **2018**, *231*, 127-137.
[60] A. Vikram, P. R. Chowdhury, R. K. Phillips, M. Hoorfar, *J Power Sources* **2016**, *320*, 274-285.
[61] T. J. Mason, J. Millichamp, T. P. Neville, A. El-kharouf, B. G. Pollet, D. J. L. Brett, *J Power Sources* **2012**, *219*, 52-59.
[62] J. B. Ge, A. Higier, H. T. Liu, *J Power Sources* **2006**, *159*, 922-927.
[63] E. Passalacqua, G. Squadrito, F. Lufrano, A. Patti, L. Giorgi, *J Appl Electrochem* **2001**, *31*, 449-454.
[64] L. R. Jordan, A. K. Shukla, T. Behrsing, N. R. Avery, B. C. Muddle, M. Forsyth, *J Appl Electrochem* **2000**, *30*, 641-646.
[65] C. S. Kong, D. Y. Kim, H. K. Lee, Y. G. Shul, T. H. Lee, *J Power Sources* **2002**, *108*, 185-191.
[66] P. Satjaritanun, J. W. Weidner, S. Hirano, Z. Lu, Y. Khunatorn, S. Ogawa, S. E. Litster, A. D. Shum, I. V. Zenyuk, S. Shimpalee, *J Electrochem Soc* **2017**, *164*, E3359-E3371.

[67] B. Marinho, M. Ghislandi, E. Tkalya, C. E. Koning, G. de With, *Powder Technol* **2012**, *221*, 351-358.
[68] J. Lee, H. Liu, M. G. George, R. Banerjee, N. Ge, S. Chevalier, T. Kotaka, Y. Tabuchi, A. Bazylak, *J Power Sources* **2019**, *422*, 113-121.
[69] T. Swamy, E. C. Kumbur, M. M. Mench, *J Electrochem Soc* **2010**, *157*, B77-B85.